A multidisciplinary study of the final episode of the Manda Hararo dyke sequence, Ethiopia, and implications for trends in volcanism during the rifting cycle

T. D. BARNIE[1,9]*, D. KEIR[2], I. HAMLING[3], B. HOFMANN[4], M. BELACHEW[5], S. CARN[6], D. EASTWELL[2], J. O. S. HAMMOND[7], A. AYELE[8], C. OPPENHEIMER[1] & T. WRIGHT[4]

[1]*Department of Geography, University of Cambridge, Downing Place, Cambridge CB2 3EN, UK*

[2]*National Oceanography Centre Southampton, University of Southampton, European Way, Southampton SO14 3ZH, UK*

[3]*GNS Science, 1 Fairway Drive, Avalon 5010, P.O. Box 30–368, Lower Hutt 5040, New Zealand*

[4]*School of Earth and Environment, Maths/Earth and Environment Building, The University of Leeds, Leeds LS2 9JT, UK*

[5]*Boone Pickens School of Geology, Noble Research Center, Oklahoma State University, Stillwater, OK 74078, USA*

[6]*Department of Geological and Mining Engineering and Sciences, Michigan Tech, 630 Dow Environmental Sciences, 1400 Townsend Drive, Houghton, MI 49931, USA*

[7]*Department of Earth Science and Engineering, Imperial College London, South Kensington Campus, London SW7 2AZ, UK*

[8]*Institute of Geophysics, Space Science and Astronomy, Addis Ababa University, Arat Kilo Campus, Addis Ababa, PO Box 1176, Ethiopia*

[9]*Present address: Laboratoire Magmas et Volcans, 5 rue Kessler, 63038 Clermont Ferrand Cedex, France*

*Corresponding author (e-mail: t.barnie@opgc.univ-bpclermont.fr)

Abstract: The sequence of dyke intrusions between 2005 and 2010 in the Manda Hararo rift segment, Ethiopia, provided an opportunity to test conceptual models of continental rifting. Based on trends up to dyke 13 in the sequence, it was anticipated that, should magma supply continue, dykes would shorten in length and eruptions would increase in size and decrease in distance from the segment centre as extensional stress was progressively released. In this paper we revisit these predictions by presenting a comprehensive overview of the May 2010 dyke and fissure eruption, the 14th and last in the sequence, from InSAR, seismicity, satellite thermal data, ultraviolet SO_2 retrievals and multiple LiDAR surveys. We find the dyke is longer than other eruptive dykes in the sequence, propagating in two directions from the segment centre, but otherwise fairly typical in terms of opening, propagation speed and geodetic and seismic moment. However, though the eruption is located closer to the segment centre, it is much smaller than previous events. We interpret this as indicating that either the Manda Hararo rifting event was magma limited, or that extensional stress varies north and south of the segment centre.

Dyke intrusion has been described as 'the quantum event of oceanic sea floor accretion' (Delaney *et al.* 1998). It is the process that initiates and maintains segmentation at rift systems once the crust is thin enough and the magma supply high enough that intrusion of dykes occurs preferentially to normal faulting for a given extensional stress (Hayward & Ebinger 1996; Buck 2004; Wright *et al.* 2006). The intrusion of dykes is also the principal mechanism by which magma is transported to

and erupted at the surface in extensional settings (Head *et al.* 1996; Delaney *et al.* 1998). In addition, it can significantly modify the temperature and strength of the surrounding lithosphere through heating (Daniels *et al.* 2014). Dyke intrusion and related extrusion is thus responsible for constructing much of the Earth's oceanic crust; controlling the transition from continental rifting to seafloor spreading; governing late-stage rift morphology; and driving eruption dynamics. An understanding of dyke intrusion is essential for understanding these processes, as well as assessing seismic and volcanic hazard in extensional settings.

Dykes at rift segments frequently occur in swarms over a timescale of years separated by quiescent periods of hundreds to thousands of years, giving rise to the 'rifting cycle' (Ebinger *et al.* 2013). Globally, rifting events occur frequently, but typically at mid-ocean ridges making them difficult to observe. There have only been three well-observed subaerial rifting events in the modern era, the Krafla Fires in Iceland (Bjornsson *et al.* 1977; Einarsson & Brandsdottir 1980), the Asal Ghoubett rifting event in Djibouti (Ruegg *et al.* 1979; Ruegg & Kasser 1987; Doubre *et al.* 2007a, b) and the Manda Hararo rifting event in northern Afar (Wright *et al.* 2006; Ayele *et al.* 2009; Grandin *et al.* 2009, 2010a, b; Keir *et al.* 2009; Ebinger *et al.* 2010). Recent events at the Manda Hararo rift provide a rare opportunity to study dyke intrusion and lava extrusion in a rift segment with the full suite of geophysical techniques available in a subaerial setting.

The Manda Hararo rift is one of the southernmost segments in the Red Sea rift system where it steps right-laterally across the Danakil Alps microplate into northern Afar, as shown in Figure 1a (Keir *et al.* 2013). The segment is transitional between continental rifting and oceanic seafloor spreading (Bastow & Keir 2011; Ferguson *et al.* 2013), and consists of a rifted central valley with a mid-segment central high containing a large collapse structure, and a significant stratovolcano, Dabbahu, at the northern end (Field *et al.* 2012a, b; Medynski *et al.* 2013). The segment can be considered transitional between the axial volcanic range morphology of the northern Afar rift segments (Erta 'Ale, Tat Ali, Alayta) and the rift valley graben morphology of southern Afar and the Main Ethiopian Rift (Bizouard *et al.* 1980; Hayward & Ebinger 1996; Field *et al.* 2012a, b). The current Manda Hararo rifting event began with the intrusion of an 80 km-long, 10 km-deep and 8 m-wide dyke running the full length of the segment between 20 September and 4 October 2005 (Wright *et al.* 2006; Ayele *et al.* 2007). This began with seismicity beneath Dabbahu at the segment tip, which then jumped to the segment centre and subsequently

propagated north and south along the rift, indicating the involvement of both central and satellite magma chambers (Ayele *et al.* 2009). Thirteen more dykes were intruded including that of May 2010, with successive dykes typically propagating in one principal direction from the segment centre, in a complex pattern that has been interpreted as a function of (1) pre-existing heterogeneities in stress along the rift, and (2) 'unclamping' by previous dyke intrusions (Hamling *et al.* 2009, 2010; Grandin *et al.* 2010a). The earthquake swarms associated with the dykes originated at the segment centre in a region approximately 5 km in radius and >6 km depth (Belachew *et al.* 2011): satellite geodesy revealed little to no deformation during intrusion except for the November 2007 and October 2008 intrusions, where a Mogi source cannot account for the volume intruded (Hamling *et al.* 2009), while between intrusion deformation has been modelled as being consistent with re-inflation of a shallow composite sill–dyke magma body and a deeper body (Grandin *et al.* 2010b; Hamling *et al.* 2014).

The advance of the dykes, as recorded by propagating seismic swarms, decreased exponentially with time, which is consistent with decreasing pressure in the source magma chamber (Rivalta 2010; Belachew *et al.* 2011; Rivalta *et al.* 2015). The August 2007 and June 2009 dykes were both associated with basaltic fissure eruptions 10 km south of the segment centre in the Karbahi graben (Ferguson *et al.* 2010) and were unusually aseismic, shallower and smaller compared with the non-eruptive dykes (Belachew *et al.* 2011).

Based on the evolution of the Krafla dyke sequence, numerical models (Buck *et al.* 2006) and the Manda Hararo dyke sequence up to dyke 13, it was proposed that as extensional stress in the rift segment is released, dykes have less of a propensity to be drawn away from the segment centre to accommodate extension; instead becoming shorter and rising vertically, resulting in eruptions of increasing size and proximity to the segment centre, provided magma supply is maintained (e.g. Ferguson *et al.* 2010). The 2007 and 2009 eruptions established a trend of increasing erupted volume and increasing ratios of extruded to intruded magma, consistent with this model. In this paper we test this prediction by integrating interferometric synthetic aperture radar (InSAR), seismicity, light detection and ranging (LiDAR) and thermal and ultraviolet satellite observations of the May 2010 dyking event.

Methods

Here we outline the InSAR and seismicity methods used to recover the dyke dimensions and timing
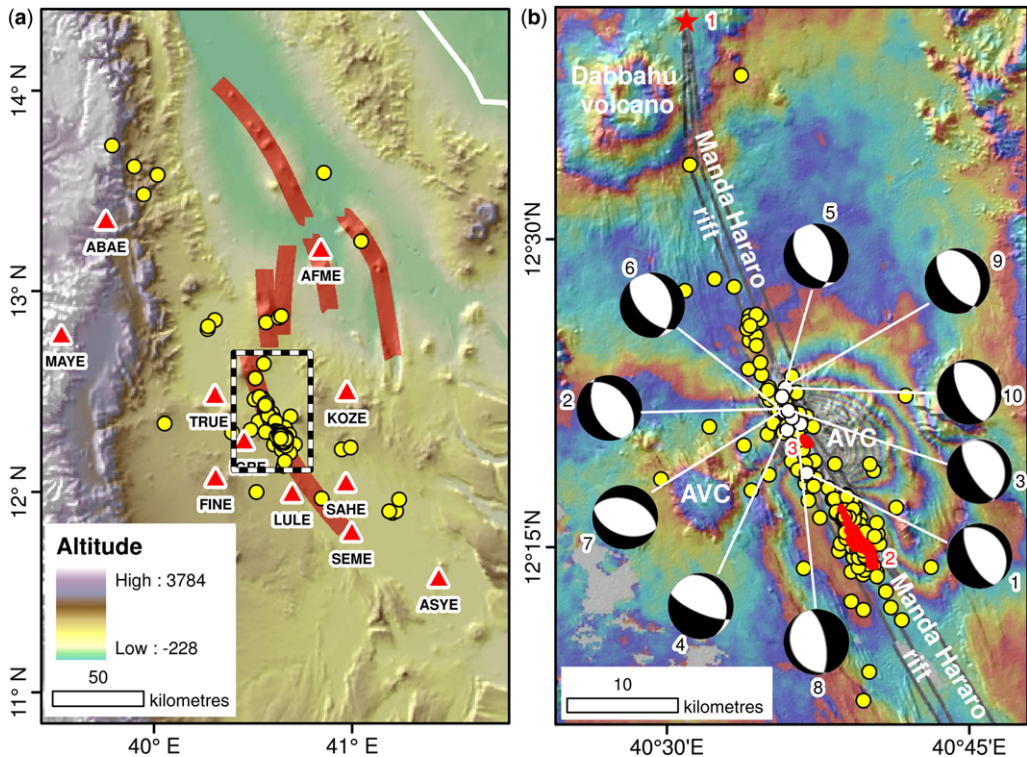
Fig. 1. (**a**) Topographic map of northern Afar with rift segments and axial volcanic ranges highlighted in red, earthquake epicentres shown as yellow dots and seismometer locations as red triangles. The chequered box gives the extent of panel (b). The topography and bathymetry are from the SRTM30 dataset (Becker *et al.* 2009). (**b**) The interferogram for the May 2010 dyke intrusion at the Manda Hararo rift segment. A single cycle from one colour back to that colour between two points indicates relative motion between those points along the radar look direction equal to one wavelength, in this case 0.028 m. Black line shows the surface trace of the dyke and fault model based on Hamling *et al.* (2009, 2010), yellow dots show earthquake epicentres, white dots show epicentres for earthquakes with moment tensor solutions. The focal mechanisms are shown and numbered as in Table 1. The eruptions that have occurred during the rifting event post-2005 are shown in red and numbered: (1) small rhyolite dome at Da'Ure emplaced during the megadyke intrusion in 2005; (2) two basaltic fissure eruptions during August 2007 and June 2009; (3) the eruption presented in this paper, the May 2010 fissure eruption. Dabbahu and the Ado Ale Volcanic Complex (AVC) are volcanic edifices.

of emplacement, the thermal and LiDAR observations of the erupted lavas and the recovery of the total SO_2 emitted using ultraviolet satellite images.

InSAR

We used two interferograms derived from Envisat Advanced Synthetic Aperture Radar (ASAR) data covering the dyke intrusion on descending tracks 464 and 49. The radar acquisitions on track 464 were on 24 April and 29 May 2013 and on 30 April and 4 June 2013 for track 49. Both of the interferograms used in this study were processed using JPL/Caltech ROI PAC software (Rosen *et al.* 2004). The topographic phase was removed using

a 3-arcsecond, 90 m resolution digital elevation model (DEM) generated by the NASA Shuttle Radar Topography Mission (SRTM) (Farr & Kobrick 2000) and a power spectrum filter was applied (Goldstein & Werner 1998). Interferograms were unwrapped using the branch-cut method of Goldstein *et al.* (1988), with errors fixed manually. To model the intrusion, we assumed the same geometry as Hamling *et al.* (2009, 2010) and performed a joint inversion of both datasets to solve for the best-fitting distributed opening model.

Seismicity and moment tensor solutions

We used seismic data recorded during May 2010 in Afar by the 2009–11 Afar 0911 network of 12

Guralp ESPD seismometers (Fig. 1a). We used Hypo2000 (Klein 2002) to locate 308 earthquakes from arrival time measurements on clear P- and S-wave arrivals filtered using a bandpass filter of 1 to 15 Hz. We employed a crustal 1D seismic velocity model constrained by the results of wide-angle seismic experiments in Afar (Makris & Ginzburg 1987), but to avoid artificial clustering of earthquakes at sharp steps in the velocity model we included a linear increase in seismic velocity within each layer (Tarasewicz *et al.* 2012). The resulting locations have average horizontal errors of <500 m and errors in depth of <2 km. Local magnitudes (M_L) of the earthquakes were computed from the maximum zero-to-peak amplitude measured on simulated horizontal component Wood–Anderson displacement seismograms after removal of instrument response (Richter 1935). These measurements were used in conjunction with hypocentral distances to estimate M_L using the distance correction applicable to the Main Ethiopian Rift (MER) (Keir *et al.* 2006), as employed in Keir *et al.* (2011). These analyses also showed that the magnitude of earthquakes ranges from M_L 0.4 to 4. Seismic moment release (Mo) is determined using the empirical relationship derived between M_L and Mo by Hanks & Kanamori (1979).

The Centroid Moment Tensor (CMT) algorithm based on that of Kao *et al.* (1998) is used to determine the source mechanisms for the largest earthquakes. The algorithm uses full waveforms from the vertical, radial and transverse components. Green's Functions for each station are calculated at an array of depths between 1 and 25 km in increments of 1 km beneath a fixed epicentre using a technique based on that of Zhu & Rivera (2002). An average 1D, layered velocity model is used. Moment-tensor inversion is performed for each trial focal depth in the depth array, and the misfit in waveform is calculated for each component of a station:

$$E_i = 1 - \frac{f_i(t)_{max}}{g_i(t)_{max}}$$
$$\times \frac{\int f_i(t)g_i(t)}{\sqrt{\int f(t)^2 dt} \times \sqrt{\int g_i(t)^2 dt}}, \qquad (1)$$

where E_i is the waveform misfit between the synthetic and the observation for each component of a given station, $f_i(t)$ and $g_i(t)$ are the amplitudes of the *i*th observed and synthetic waveforms, respectively, while $f_i(t)_{max}$ and $g_i(t)_{max}$ are the maximum amplitudes of these waveforms. E_i ranges from zero (perfect match) to two (extreme mismatch). Misfit values for all the components from all the stations considered are combined to form an average waveform misfit (E_{ave}) at a given trial hypocentre:

$$E_{ave} = \frac{\sum_{i=1}^{N} E_i}{N}, \qquad (2)$$

where N is the number of components used. From this a misfit-depth function is generated, and the moment tensor and hypocentre related to the minimum average misfit is considered to represent the best source mechanism estimate.

We selected local earthquakes for CMT analysis that had a magnitude of more than three. In addition, a minimum of six stations was considered for the source inversion based on visual inspection of waveform quality and azimuth of the station with respect to the earthquake. A layered 1D *P*-wave velocity model of Jacques *et al.* (1999) derived from earlier seismic refraction studies in Afar (Makris & Ginzburg 1987) and V_p/V_s ratio of 1.8 determined from regression of travel times (Belachew *et al.* 2011) were used. To minimize the effect of the oversimplified velocity model and variation in the noise level at each station, the solutions were tested using three bandpass filters: 0.02–0.06, 0.03–0.08 and 0.05–0.1 Hz. The bandpass filter between 0.03 and 0.08 that resulted in a minimum average misfit among the three is chosen for all the events considered. The CMT solutions for ten events are given in Table 1.

Satellite measurements of SO₂ emissions

SO_2 emissions associated with the 21 May 2010 eruption in the Manda Hararo rift were detected from space by the Global Ozone Monitoring Experiment 2 (GOME-2) aboard the MetOp-A satellite and the Ozone Monitoring Instrument (OMI) aboard NASA's Aura satellite. GOME-2 and OMI are hyperspectral ultraviolet (UV)/Visible spectrometers with sensitivity to lower tropospheric SO_2 emissions. Infrared satellite instruments that have poor sensitivity to the lower troposphere, such as the Atmospheric Infrared Sounder (AIRS) on Aqua and the Infrared Atmospheric Sounding Interferometer (IASI) on MetOp-A, detected no SO_2 during the eruption, from which we infer a plume altitude of less than 5 km.

For our analysis we use the operational SO_2 products derived from each satellite instrument. GOME-2 SO_2 data were obtained from the Support to Aviation Control Service (SACS; Brenot *et al.* 2013), which archives daily GOME-2 SO_2 retrievals (e.g. Rix *et al.* 2009; SACS 2012). AIRS and IASI SO_2 data were also examined using the SACS data archive. The operational OMI

Table 1. *Selected moment tensor solutions*

Event	Date (year/month/day)	Time (UT)	Lat. (°N)	Lon. (°E)	Depth (km)	M_w	Strike	Dip	Rake
1	2010/05/20	22:04:47	12.309	40.617	1.0	3.28	324/154	25/64	−98/ − 85
2	2010/05/21	00:45:56	12.359	40.604	1.0	3.3	318/157	41/49	−104/ − 77
3	2010/05/21	01:44:46	12.349	40.612	1.0	3.7	351/148	23/67	−69/ − 99
4	2010/05/21	02:02:55	12.344	40.601	3.0	3.6	339/114	24/72	−47/ − 107
5	2010/05/21	02:23:45	12.359	40.599	3.0	3.7	142/353	45/48	−112/ − 68
6	2010/05/21	03:14:05	12.354	40.605	1.0	3.4	352/137	40/54	−62/ − 111
7*	2010/05/21	04:47:00	12.360	40.602	??	3.5	290/108	43/46	−88/ − 91
8	2010/05/21	04:29:55	12.374	40.598	1.0	3.4	155/350	23/66	−103/ − 84
9	2010/05/21	03:55:49	12.378	40.600	1.0	3.6	342/143	32/58	−73/ − 100
10	2010/05/21	03:35:50	12.371	40.597	3.0	3.4	330/154	25/64	−93/ − 88

*The error for event 7 is large and the parameters should be treated with caution.

SO_2 product is publicly available from NASA (2014) and provides vertical column amounts of SO_2 retrieved using the operational OMI SO_2 algorithm (Yang *et al.* 2007).

Airborne LiDAR

Two high-resolution airborne LiDAR datasets were acquired in October 2009 and November 2012 covering the central section of the Manda Hararo rift segment. From both datasets we generated DEMs of 0.5 by 0.5 m pixel resolution with a vertical accuracy better than 0.2 m. The change in height between the two surveys attributable to lava flow emplacement was calculated by subtracting the pre-eruption surface from the corrected post-eruption surface. We corrected the post-eruption surface by removing the dyke-induced uplift signal (0.2–0.3 m). This was done by fitting a linear regression plane to the fault block hosting the eruption, excluding the new lavas, and subtracting it from the surface.

Thermal remote sensing

We used thermal observations from two spaceborne sensors, the Advanced Land Imager (ALI) aboard NASA's EO-1 satellite (Ungar *et al.* 2003; Davies *et al.* 2006) and SEVIRI aboard EUMETSAT's Meteosat satellite (Aminou 2002). The ALI instrument collects images in nine bands in the visible to short-wave infrared sampled at 30 m intervals and one band in the panchromatic at 10 m, and can thus resolve geomorphological and high temperature features at sub-lava-flow scales. The satellite is in a low Earth orbit with a repeat period of 16 days. Here, we use an image acquired at 07:19 UTC on 22 May 2010, the first acquired after the eruption, to capture the final extent of the lava flow and show that the whole region of elevation

change captured by the LiDAR surveys was anomalously hot and can be confirmed as emplaced lava. The SEVIRI instrument collects images in 11 bands across the visible and thermal spectrum sampled at 3 km intervals and one band at 1 km, with resolution decaying to the edge of the image of the Earth disc. The satellite is in a geostationary orbit and collects an image once every 15 min, capturing the variation in total radiant output of an eruption in great detail, and with a consistent view geometry, making successive measurements in a given pixel directly comparable.

The signal received at the SEVIRI sensor is a function of reflected and scattered sunlight from the ground, cloud and atmosphere, and thermal emission from the ground, cloud, hot lava and atmosphere, and we extract the volcanic thermal signal from this mixture using Independent Component Analysis (ICA) (Hyvarinen *et al.* 2001; Stone 2004), as shown in Barnie & Oppenheimer (2015). ICA is similar to Principal Component Analysis, except that instead of decomposing the radiance time series into linearly uncorrelated components we extract components that are statistically independent of each other by maximizing their non-Gaussianity. The assumptions of independence and non-Gaussian distribution prove sufficient to isolate the thermal signal from other processes contributing to the signal at the sensor. In this study we use ICA to extract the volcanic thermal signal from the short-wave infrared (1.6 μm) and mid-infrared (3.9 μm) channels. The short-wave infrared is pre-processed by finding linear relationships with other bands lacking thermal anomalies and subtracting the predicted radiance to suppress the background, making it easier for the ICA algorithm to isolate the volcanic signal. The mid-infrared is corrected for saturation effects by excluding saturated pixels from the ICA algorithm under the assumption that neighbouring pixels faithfully record the
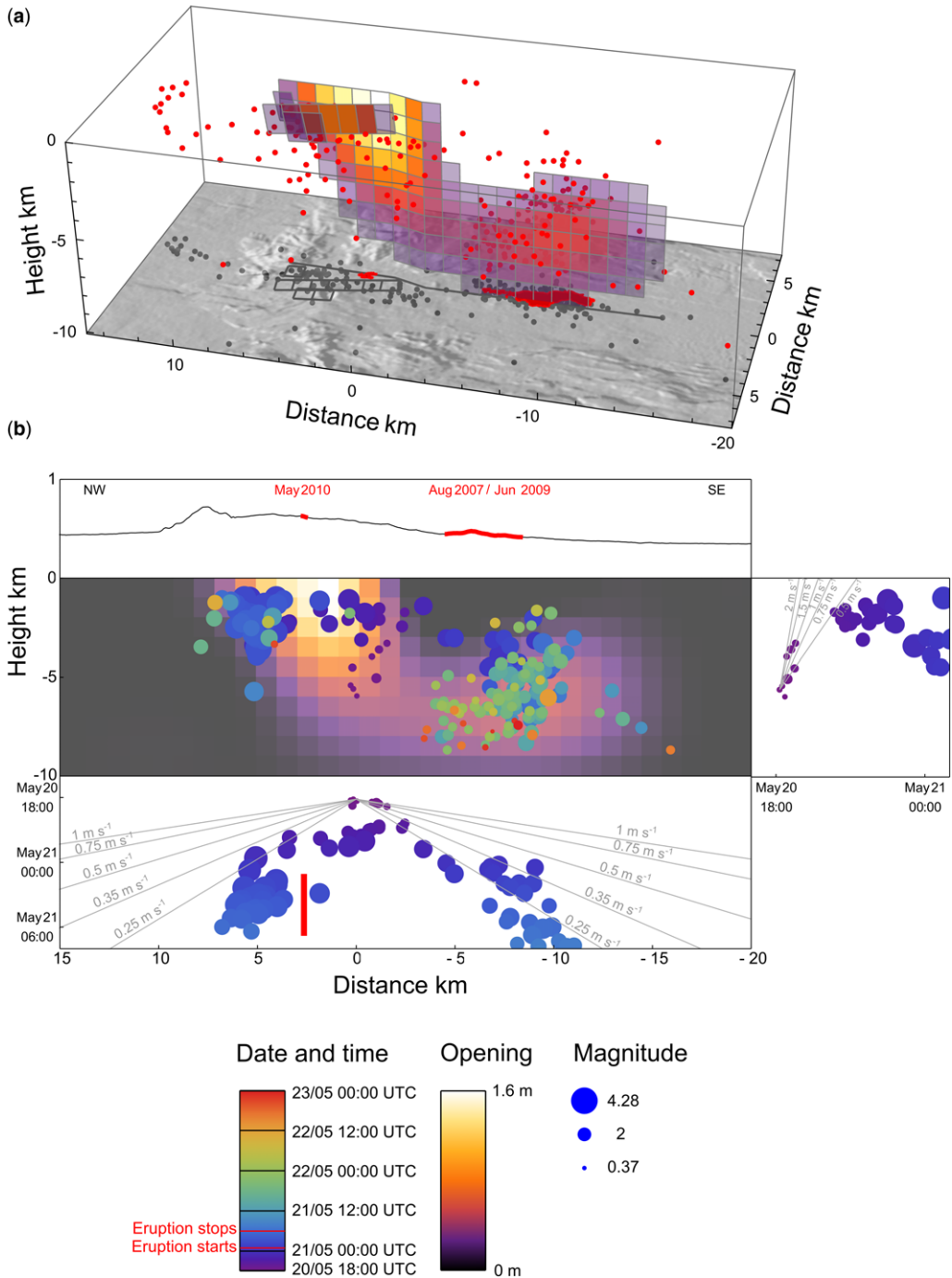
(a)

(b)

Fig. 2. (**a**) A perspective plot of modelled dyke opening, fault displacement and seismicity. Earthquake foci are shown as red dots. The projection of the deformation model grid and seismicity is shown onto a hill shade of SRTM topography. Distances are given rift perpendicular and rift parallel, centred on the first earthquake of the dyke intrusion sequence. (**b**) A space–time plot showing the distribution of opening along the dyke and the time evolution of seismicity. The top panel shows the topographic profile along the dyke, with sections that emitted lava during this intrusion (May 2010) and previous intrusions (August 2007 and June 2009) highlighted. The middle panel shows the

same signal at a lower amplitude, thus avoiding saturation.

Results

InSAR and seismicity

The InSAR and seismicity data show the dyke was intruded along the same axis as the earlier dykes in the sequence (see Hamling *et al.* 2009; Belachew *et al.* 2011), with the seismicity lying mostly within the axial graben-bounding faults of the deformation model used by Hamling *et al.* (2009, 2010) to model fault slip associated with earlier intrusions (Fig. 1). The distribution of opening inferred along the model by inverting the interferograms reveals the intrusion of two dyke segments north and south of the rift segment centre, each with a separate locus of maximum opening, as shown in Figure 2. The model predicts maximum opening of 1.6 m near the surface in the northern segment below the eruption site, with opening of up to 1 m occurring down to 4 km. An opening of *c.* 0.5 m is predicted in the southern segment at depths of between 5 and 9 km. The volume intruded by the dyke was 0.081 km^3 and produced a geodetic moment of 3.216×10^{18} N m, over two orders of magnitude larger than the total seismic moment of 9.37×10^{15} N m, indicating the majority of the dyke emplacement was accommodated aseismically, as occurred during previous events (Belachew *et al.* 2011).

The seismicity is mostly contained within the region of significant opening, with the exception of a region at the segment centre that is largely aseismic. This aseismic region has been observed by previous authors (Belachew *et al.* 2011) and attributed to the presence of a shallow magma chamber or hot weak crust, consistent with it being the source region for dykes propagating north and south. Seismicity in the northern dyke segment extends from the surface down to roughly 6 km, while seismicity in the southern segment spans a depth range of 2–9 km, and in both cases is mostly confined to the region of significant opening revealed by InSAR observations. Earthquakes for which CMT solutions are available are all shallow (1–3 km depth), in the northern dyke segment, and consistent with extension slip on shallow normal faults (Fig. 2).

Earthquake depths constrained in the moment tensor inversion are consistent with the depths of the same earthquakes achieved during earthquake location.

Lava flow geomorphology

The eruption site has not been visited by any geoscientists, and the authors have been unable to find eyewitness accounts of the eruption itself, or of the lava flow post-emplacement, so the geomorphological interpretation is drawn from the difference between two LiDAR surveys and an ALI multispectral image, as shown in Figure 3. The difference between the before and after eruption DEMs reveals the thickness of the new material emplaced or removed. The positive topographic anomaly matches the thermal anomaly recorded in the short-wave infrared in the ALI image acquired 07:19 UTC 22 May 2010, showing that all of the new topography was emplaced as hot volcanic material. The eruption appears to consist of two lava flows, one situated on the footwall of a normal fault, which consists of a lava flow up to 2 m thick, sourced from a fissure about 600 m long, interspersed with low scoria cones and ramparts less than 2 m high. The southern end of the fissure terminates before the fault scarp, and below the fault scarp on the hanging wall is a second lava flow that appears disconnected from the first. This second flow abuts and follows the fault scarp; however, it is difficult to make out the source and direction of flow from the geomorphology as revealed by the LiDAR: there are no channelization features, and the flow surface is very smooth compared to the footwall flow. A plausible source is through the fault itself, perhaps through the collapse features revealed as a negative change in topography. The southernmost end of the fissure above the fault scarp and the entire lava flow below it exhibit higher radiance in the ALI image than the rest of the fissure and flow. This could be due to the material having been emplaced last and so still being hot. However, the image is acquired a full day after the eruption, which itself lasted only 6 h, and variation in surface temperature after a long interval is more a function of surface type (aa/pahoehoe) with smoother surfaces retaining heat, so this may indicate that the emplacement of the southern flow was a less intense eruption of pahoehoe lava.

Fig. 2. (*Continued*) distribution of openings on the face of the dyke, and the location of seismicity projected onto the dyke. All seismicity between 20 May 12:00 UTC and 23 May 00:00 UTC and within 3 km of the dyke is shown, with size proportional to magnitude and colour to date and time. The right and lower panels show the vertical and horizontal propagation of the seismicity during the first 6 and 12 hours, respectively. Isotachs of constant velocity are shown in grey, and the period of lava emission is shown as a red line. Note that seismicity originates at the centre of the segment, migrates upwards, then laterally and then down.
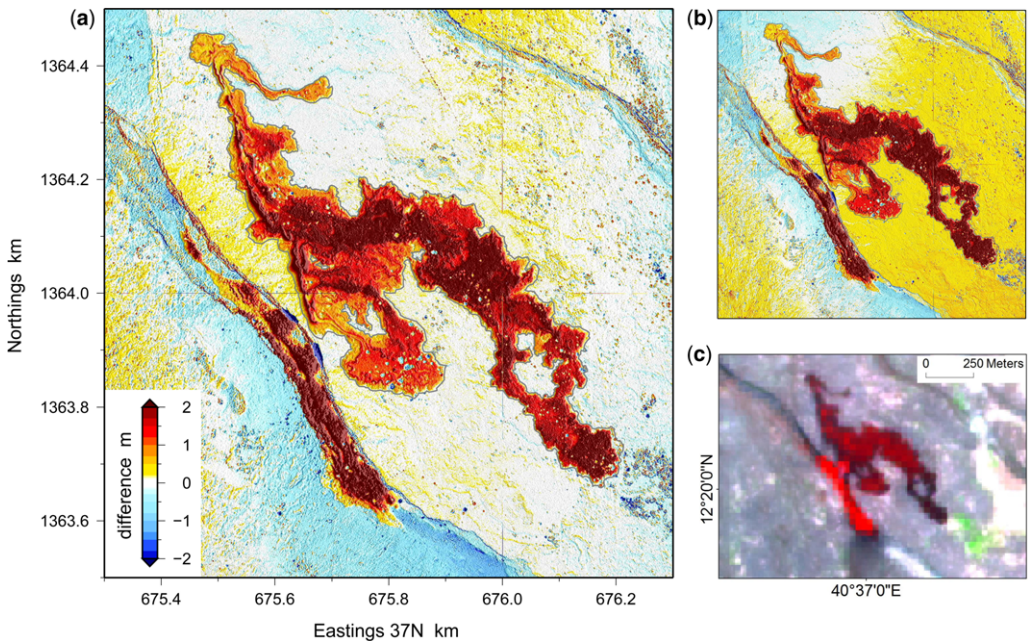
Fig. 3. (**a**) The change in height between pre- and post-eruption LiDAR surveys, after correction for footwall uplift. An increase in height appears red, a decrease appears blue and no change appears white. Two lava flows are present, one on the northern footwall of the prominent normal fault, sourced from a NNW–SSE-trending fissure and one on the hanging wall to the south. Note the blue patches on the fault scarp showing the location of rockfalls, and blue areas on the lava flow probably representing canopies of bushes engulfed and burned by the lava flow. (**b**) The change in height between the two LiDAR surveys before the correction for uplift of the footwall is applied. Note the broad region of uplift of <1 m in the east of the map. (**c**) ALI image acquired 07:19 UTC 22 May 2010, showing bands 9, 8 and 7 (2.2, 1.6 and 1.25 μm) as RGB, respectively. High residual temperatures in the erupted material appear red, confirming that positive topography in the LiDAR-difference image was emplaced as hot material. Note highest temperatures at southern end of the fissure and in southern lava flow, which may represent younger material or a different surface type.

SEVIRI thermal observations and effusion rates

The onset of the eruption can be seen in both the 1.6 and 3.9 μm wavebands between 00:57 UTC and 01:12 UTC on 21 May 2010, while the signal drops to zero by 06:00 UTC at 1.6 μm and decays slowly over the next 24 h at 3.9 μm (Fig. 4). We interpret this difference in waning signal as a function of the non-linear relationship between temperature and radiance at different wavelengths such that shorter wavelengths are more sensitive to the hotter temperatures of freshly exposed material, while longer wavelengths are more sensitive to lower temperatures of older material, and thus are a measure of freshly exposed material and older cooling material (e.g. Davies *et al.* 2010). In other words, we can think of the radiance at short wavelengths as a function of the instantaneous rate of emplacement of hot material, and a convolution of that rate at longer wavelengths. We therefore take the short-wave radiance as some measure of the

rate of exposure of fresh hot material within the field of view of the instrument. If we assume that there is a linear relationship between the effusion rate, rate of exposure of hot material, and radiance, we can normalize the short-wave radiance curve by the total volume of erupted material to give an estimate of the effusion rate. This gives a peak effusion rate of 24 m^3s^{-1}.

Sequence of events

By integrating observations from seismicity and satellite thermal observations we can reconstruct the sequence of events during the dyke intrusion and eruption. In the following section the positions of events are given relative to the dyke as 'north' and 'south' referring to directions along the strike of the dyke on to which earthquake locations are projected. Times are in UTC.

Prior to the intrusion, between the 17 and 19 May, there was some minor seismicity (M_L 1–1.6) along the rift axis to the north of the May 2010
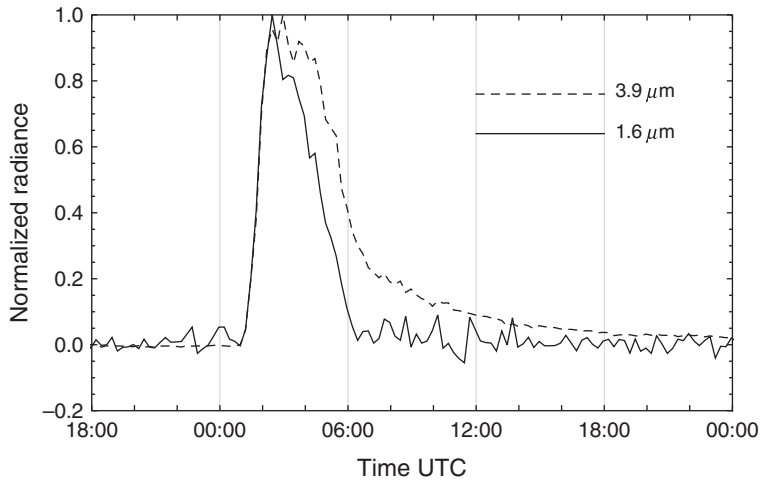
Fig. 4. Time series of radiant output from the May 2010 eruption extracted using ICA. The dashed line shows the 3.9 μm signal (after Barnie & Oppenheimer 2015) and the continuous line shows the 1.6 μm signal. Note that the 3.9 μm signal takes longer to decay to zero, which is a function of the signal being more sensitive to lower temperatures and thus picking up a cooling signal from the lava flow after emplacement. The 1.6 μm signal is only sensitive to the hottest temperatures, and so more faithfully tracks the rate of exposure of fresh hot material, which we take as a proxy for effusion rate.

dyke intrusion. The initiation of the dyke injection is revealed by a cluster of M_L 0.6–1.37 earthquakes on the 20 May between 18:09 and 18:47 located at the segment centre (Fig. 2b) that progressively shallow through time from 5.6 to 3.5 km. The low density of the earthquakes makes estimating propagation speeds difficult, but by plotting the seismicity over isotachs (lines of constant speed), the propagation speed can be estimated to the first order (Fig. 2b), giving a vertical motion of magma on the order of approximately 1 m s^{-1}. After a brief hiatus, earthquake activity recommences at 20:21 and is characterized by the simultaneous migration of seismicity north and south by approximately 8 and 10 km, respectively, reaching their maximum northerly and southerly extents at roughly 00:00 and 08:00, respectively, on 21 May, and giving northerly and southerly mean propagation speeds on the order of 0.35 and 0.25 m s^{-1}, respectively (Fig. 2b). During the propagation of the of the dykes north and south, the range of earthquake magnitudes rises to M_L 2 to 4, with the majority of the seismic moment being released between 20 May 22:00 and 21 May 05:00 in the northern dyke segment, and 35% of the total moment released by a single earthquake of M_L 4.28 at 3:13 on 21 May (Fig. 5).

The eruption began between 00:57 and 01:12 on 21 May, after the northern dyke appears to have reached most of its final extent, with effusion rates rising to a peak of around 24 m^3 s^{-1} at around 02:27 and dropping to zero by 06:27. The eruption

coincides with a cluster of earthquakes that range from M_L 2.7 to 4.28, occurring to the north of the eruption site. This cluster contains nine of the 10 events for which CMT solutions are available (see Fig. 1b, Table 1), with M_L 3.3–3.7, depths between 1 and 3 km and solutions consistent with slip on shallow normal faults. The frequency of earthquakes drops rapidly at the end of the eruption. In contrast, in the southern dyke segment, seismicity persists until the morning of 22 May, with magnitudes dropping to approximately 1 (Fig. 5), and seismicity migrating to greater depths and back towards the centre during late 21 May and early 22 May (Fig. 2b).

The peak in seismic moment release during earthquake migration is consistent with the earthquakes being generated by localized extensional stresses near the tip of the propagating dyke (Roman & Cashman 2006). Earthquake magnitudes are greatest at the latter stages, or just after the end, of dyke growth, as noted for earlier dykes in the Manda Hararo sequence by Grandin *et al.* (2011), who explained this by a combination of growth of a seismogenic 'process zone' at the dyke tip and halting of dykes by inelastic deformation such as faulting. After the dyke stops propagating, there is no longer a mechanism for inducing large stress changes, but low magnitude earthquake activity continues around the stalled dyke tip perhaps due to small-scale faulting in response to processes such as dyke cooling, induced fault-related stress changes, or small volumes of continued intrusion
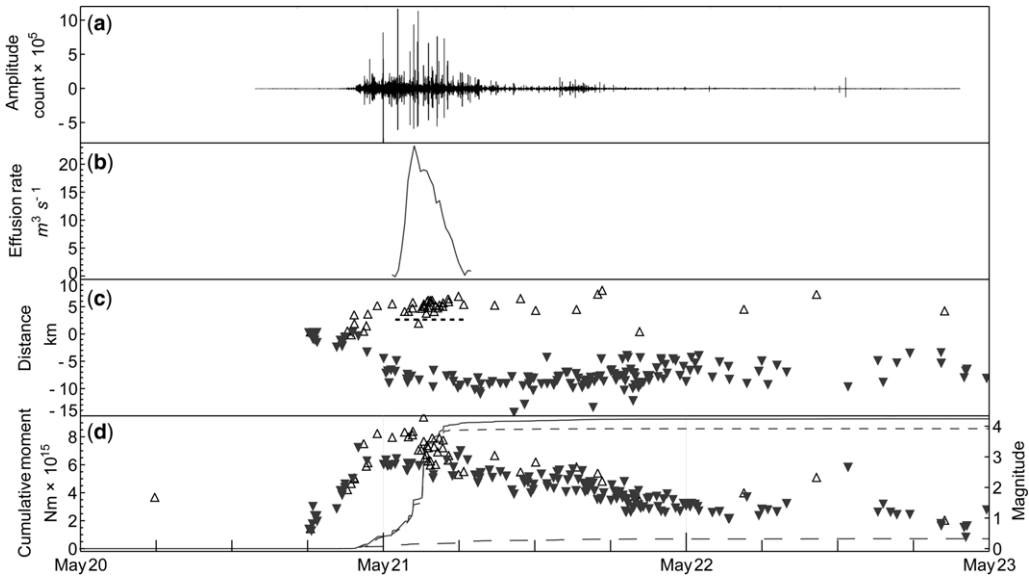
Fig. 5. The timing of seismic events and lava effusion. (**a**) Vertical component seismic trace for station IGRE (see Fig. 1a). (**b**) Effusion rate calculated from extracted SEVIRI band 3 (1.6 μm) radiance. (**c**) Migration of seismicity along dyke by distance from centre. Open triangles are northern segment earthquakes, filled triangles southern segment earthquakes and dashed line shows location and duration of the eruption. All earthquakes within 3 km of the dyke are plotted. (**d**) Earthquake magnitudes and cumulative moment for all events within 3 km of the dyke model. Open triangles are earthquakes in the northern dyke segment, filled triangles are earthquakes in the southern dyke segment, short dashed line shows cumulative seismic moment for northern dyke, long dashed line is for southern dyke and the continuous line gives the total.

into the already opened dyke. The seismic moment release associated with the dyke north of the segment centre is larger than that to the south: this may be due to the shallower northern dyke triggering faulting in cooler rock close to the surface that is more susceptible to brittle fracture, as well as due to the larger volume of the northern dyke.

In summary, the seismicity data suggest the dyke was intruded in two segments. The first propagated laterally 8 km north during 18:09 20 May to 00:00 21 May and was associated with an eruption in the period 01:00 to 06:27 21 May with peak effusion at 02:27 h, after which the frequency of earthquakes drops off rapidly. The second dyke propagated 10 km southward in the interval 18:09 20 May to 08:00 21 May, after which seismicity migrated downwards and back towards the segment centre while slowly decaying in frequency and magnitude.

Mass balance for sulphur emission

GOME-2 detected SO_2 immediately SE of the eruption site at 6:54 on 21 May (approximately 6 h after onset of the eruption), which is apparent on SO_2 images produced by SACS (SACS 2010; Brenot

et al. 2013). The SO_2 column amounts were too low and localized to trigger an SO_2 alert by the SACS system. However, daily GOME-2 SO_2 retrievals (e.g. Rix *et al.* 2009) available from SACS (2012) indicate two clearly anomalous (i.e. above background) pixels containing 9.2 and 7.4 Dobson Units (DU) of SO_2 (1 DU = 2.69×10^{16} molecules cm^{-2}), assuming a lower tropospheric SO_2 plume altitude of approximately 2.5 km. Using the GOME-2 pixel dimensions of 80 km × 40 km, these column amounts yield a total SO_2 mass of approximately 1.5 Gg. Adjustment for a small background noise offset of 1–2 DU would reduce this amount to approximately 1.15–1.3 Gg. OMI SO_2 measurements at 11:21 UTC on 21 May confirm the presence of volcanic SO_2. Column amounts retrieved using the operational OMI SO_2 algorithm (Yang *et al.* 2007), also assuming a *c.* 2.5 km plume altitude, yield a total SO_2 mass of *c.* 0.9 Gg. The difference between the GOME-2 and OMI SO_2 measurements may be explained by SO_2 removal (e.g. via oxidation or deposition) in the 4.5 h between satellite overpasses and also to the OMI row anomaly (OMI Row Anomaly Team, 2012), a data gap, which may have obscured some of the SO_2 cloud. Neither GOME-2 nor OMI

measured significant SO_2 amounts above background on the following day, confirming the short timescale and low magnitude of the event.

The SO_2 emission can be used to estimate the volume of magma that degassed to produce it based on an assumed sulphur content of the melt before and after eruption. Following Ferguson et al. (2010), we take this value as 900 ppm by mass of S in the melt. The range of 1.15–1.3 Gg of SO_2 then suggests derivation from a magma volume of $0.26–0.29 \times 10^6$ m^3 (based on a density of 2500 kg m^{-3} and without accounting for crystal fraction). The differenced DEMs indicate a total emplaced lava volume of 0.23×10^6 m^3. Given the uncertainties in the key parameters (notably sulphur content available for degassing and the density of the emplaced lava flow), the similarity between the volumes suggests that degassing of the erupted lava can account for the emitted SO_2. Ferguson et al. (2010) reached the same conclusion for the earlier eruptions on the rift. The volume of the dyke modelled from the InSAR geodetic signal is 0.081 km^3, nearly two orders of magnitude greater than the volume of erupted lava. The low ratio of erupted to unerupted magma breaks the trend of increasing ratios from the 2007 and 2009 Manda Hararo fissure eruptions expected if the rift cycle is following the same pattern as Krafla (Ferguson et al. 2010).

Discussion

Seismicity reveals the dyke initiated in the (relatively) aseismic centre of the segment at around 6 km depth on 18:09 20 May, propagating at speeds of 0.25–0.35 m s^{-1} laterally and 1 m s^{-1} vertically. The initial vertical propagation of the dyke involves some seismicity in an otherwise aseismic region (as noted for other intrusions, e.g. Belachew et al. 2011), and the seismicity in this region during the May 2010 dyke intrusion is (1) only during the initial injection, and (2) only tracking the vertical motion at the very centre, which is consistent with the seismicity tracking the propagation of the tip during the initial stages of dyke propagation (Keir et al. 2009; Dahm et al. 2010; Belachew et al. 2011). Seismicity propagates north and south from the segment centre, emplacing two dyke segments of approximately 8 and 10 km length, which show differing final geometries and variations in seismicity.

The northern dyke is shallow, extending from the surface to 6 km depth with a maximum opening of 1.6 m near the surface. Seismicity suggests that it propagates faster than the southern dyke and produces an eruption after northward propagation has (mostly) finished. The majority of the seismic moment is released during the eruption, and seismicity almost ceases after the eruption stops.

In contrast, the southern dyke extends from 2 to 9 km. The migration of seismicity suggests that it propagates more slowly and there is no eruption associated with the intrusion. Seismicity continues for a day after seismicity at the northern segment has stopped and propagates downwards before migrating back towards the segment centre during emplacement of the southern dyke. It is unclear whether this back-propagation of seismicity represents dyke propagation or represents seismic activity in a previously aseismically intruded region. Comparing the distribution of seismicity with the distribution of opening, the latter scenario seems more likely than the dyke propagating by the tortuous route mapped out by the seismicity.

One explanation for the difference in behaviour between the two dykes is that the eruption in the northern segment 'depressurizes' the dyke, resulting in an end in seismicity after the eruption stops, whereas seismicity in the still-pressurized southern segment continues. However, the volume of the physically erupted lava is almost two orders of magnitude smaller than the volume of intruded material, and the mass of the SO_2 cloud can more or less be accounted for by degassing of the erupted lava, so it seems unlikely that the eruption of these comparatively low amounts of lava and gas had a significant impact on the dyking process. By the start of the eruption the dyke is nearly at its full northerly extent, and the magnitude of the earthquakes peak during the eruption and are mostly shallow (those with CMT solutions indicating extensional normal faults) so the earthquakes could be tracking the response of the shallow normal fault systems to stresses imparted by the final vertical intrusion and widening and narrowing of the vent over the course of the eruption. Alternatively, both the shallow earthquakes and evolution of the vent could be reflecting broader late-stage dyke intrusion at shallow levels.

Comparison with expectations based on previous Manda Hararo dykes, the Krafla rifting event and theoretical considerations

The May 2010 dyke is consistent with the sequence of dykes in the Manda Hararo rift so far, as shown in Figure 6. Like the other dykes associated with eruptions, it has a relatively low volume and low geodetic and seismic moments. The maximum dyke opening is larger than the previous two eruptive dykes and more similar to the average opening of non-eruptive dykes. The larger opening coupled with longer length due to the two dyke segments north and south of the rift centre results in a
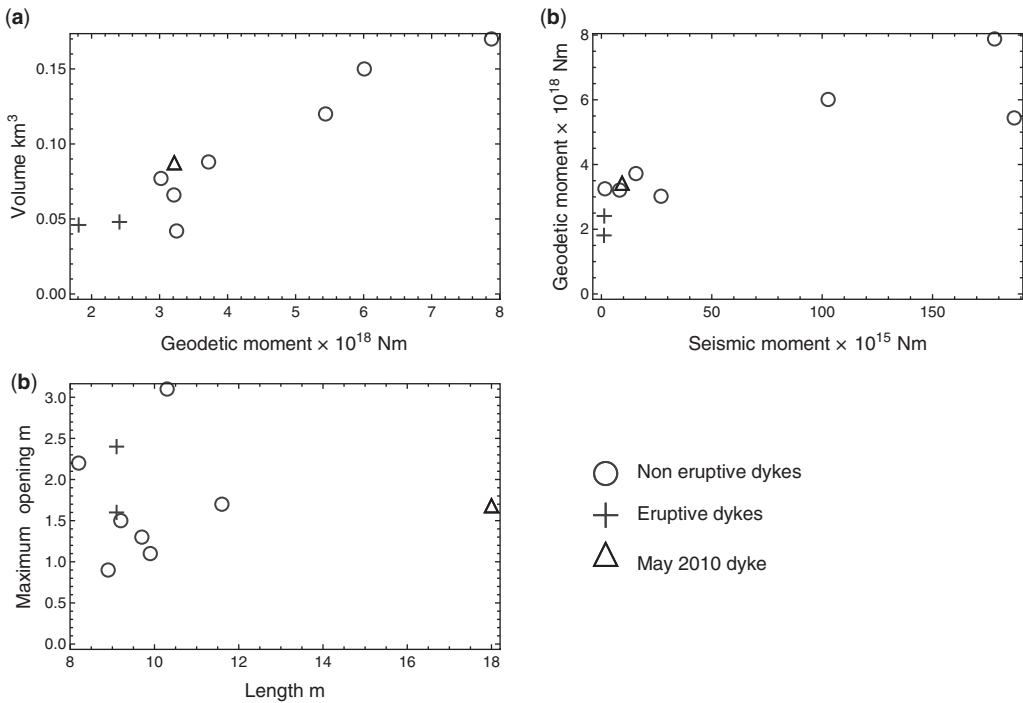
(a)

(b)

(b)

○ Non eruptive dykes

+ Eruptive dykes

△ May 2010 dyke

Fig. 6. Comparison of May 2010 dyke volume and moments with data available for dykes 2, 3, 7, 8, 9, 10, 11, 12 and 13 in the Manda Hararo sequence. Data from Belachew *et al.* (2011) and Hamling *et al.* (2009, 2010). (**a**) Volume of dyke against geodetic moment. (**b**) Dyke maximum opening against length. (**c**) Geodetic moment against seismic moment.

larger volume than the previous two eruptive dykes. Estimates of mean dyke propagation rates from seismicity for dykes with eruptions are not reported by Belachew *et al.* (2011) due to their low seismicity; however, our order of magnitude estimates (0.25 and 0.35 m s^{-1} horizontally) are consistent with the range reported for non-erupting dykes (0.16–0.75 m s^{-1}). Compared to previous eruptions, the May 2010 fissural flows are much smaller with a volume of 0.23×10^6 m^3, compared to estimates of 4.4×10^6 m to 8.8×10^6 m^3 and 13×10^6 m to 18×10^6 m^3 for the August 2007 and June 2009 eruptions, respectively (Ferguson *et al.* 2010), giving an intrusive to extrusive ratio of 360:1, a decrease on 10:1 and 5:1 for the 2007 and 2009 events. The mean effusion rate for the May 2010 eruption is also substantially lower, 12.5 m^3 s^{-1} compared with estimated mean effusion rates of 55 and 70 m^3 s^{-1} for 2007 and 2009, respectively. Finally, the 2007 and 2009 lavas erupted from the same lineations of fissures around 10 km from the aseismic zone at the segment centre from which dykes propagate, whereas the May 2010 eruption occurred approximately 2 km north of the segment centre and at approximately 200 m higher elevation.

The subaerial rifting event at Krafla during the period 1975–84 culminated in a significant increase in erupted volumes during dyke injection (e.g. Tryggvason 1984). This observation has been explained by a progressive decrease in extensional tectonic stress during the episode, with later dykes more likely to erupt, since insufficient extensional stress is available to drive complete subhorizontal propagation and intrusion (Buck *et al.* 2006). As a result, surplus magma reaches the surface closer to the magma chamber and in larger volumes. While an increase in eruptive behaviour of dykes has been observed during the Dabbahu rifting episode, the total eruptive volume remains far smaller than that observed during the Krafla rifting episode. This could indicate either that significant extensional tectonic stress remains within the Dabbahu segment or that magma supply has diminished. Alternatively, the small volume and duration of the May 2010 eruption compared to the August 2007 and June 2009 eruptions may be explained by greater extensional stress to the north of the segment centre, as proposed by Grandin *et al.* (2010*a*). The greater intrusive volume of northern dykes v. the greater extrusive volume of southern dykes may simply reflect a greater amount of

extension to be accommodated north of the segment centre, leaving little magma left over for extrusion. Additionally, the higher elevation of the May 2010 eruption site may result in magma being intruded in the north that could have reached the surface had the dyke propagated south.

Conclusions

In summary, the May 2010 Manda Hararo dyke is the 14th, and perhaps last, in the Manda Hararo rifting sequence that started in September 2005, giving a rift cycle length of 4 years and 9 months. The dyke mostly falls within the range of parameters (volumes, seismic and geodetic moment, maximum opening) of previous dykes in the series and was intruded along the same axis. The dyke takes the form of a northern and southern segment propagating away from a mostly (but not initially) aseismic central zone, as observed for previous dykes and, like earlier eruptive dykes, was relatively aseismic. The northern and southern dyke segments exhibit different patterns in seismicity and opening with time and space, which may be related to the eruption in the north, a function of local residual stresses from previous dyke intrusions in the sequence, or a function of differences in extensional stress north and south of the segment centre.

The May 2010 episode does not follow the pattern of increasing extrusive to intrusive ratios seen at Krafla (Tryggvason 1984) or modelled by Buck *et al.* (2006), or anticipated subject to sustained magma supply by Ferguson *et al.* (2010); however, the eruption did occur closer to the rift centre. This might be expected once extensional stress has been relieved and is no longer diverting magma laterally: however, the dyke was unusually long. In this case, the eruption occurring close to the centre may be more a function of the patterns of extensional stress just happening to provide a path of least resistance to the surface near the magma chamber. The low volume of erupted material may indicate that the rift cycle was ultimately magma limited, and extrusion stopped due to inadequate magma supply before the extensional stress was fully relieved, or it may reflect differing eruptive styles north and south of the segment centre due to differing crustal stresses.

References

AMINOU, D. M. A. 2002. MSG's SEVIRI instrument. *ESA Bulletin-European Space Agency*, **111**, 15–17.

AYELE, A., JACQUES, E. *ET AL.* 2007. The volcano-seismic crisis in Afar, Ethiopia, starting September 2005. *Earth and Planetary Science Letters*, **255**, 177–187.

AYELE, A., KEIR, D. *ET AL.* 2009. September 2005 megadike emplacement in the Manda-Harraro nascent oceanic rift (Afar depression). *Geophysical Research Letters*, **36**, L20306, http://dx.doi.org/10.1029/2009 gl039605

BARNIE, T. & OPPENHEIMER, C. 2015. Extracting high temperature event radiance from satellite images and correcting for saturation using Independent Component Analysis. *Remote Sensing of Environment*, **158**, 56–68.

BASTOW, I. D. & KEIR, D. 2011. The protracted development of the continent–ocean transition in Afar. *Nature Geoscience*, **4**, 248–250.

BECKER, J. J., SANDWELL, D. T. *ET AL.* 2009. Global bathymetry and elevation data at 30 arc seconds resolution: SRTM30_PLUS. *Marine Geodesy*, **32**, 355–371, http://dx.doi.org/10.1080/014904109032 97766

BELACHEW, M., EBINGER, C., COTÉ, D., KEIR, D., ROWLAND, J. V., HAMMOND, J. O. S. & AYELE, A. 2011. Comparison of dike intrusions in an incipient seafloor-spreading segment in Afar, Ethiopia: seismicity perspectives. *Journal of Geophysical Research*, **116**, B06405, http://dx.doi.org/10.1029/2010jb00 7908

BIZOUARD, H., BARBERI, F. & VARET, J. 1980. Mineralogy and petrology of Erta Ale and Boina Volcanic Series, Afar Rift, Ethiopia. *Journal of Petrology*, **21**, 401–436.

BJORNSSON, A., SAEMUNDSSON, K., EINARSSON, P., TRYGGVASON, E. & GRONVOLD, K. 1977. Current rifting episode in north Iceland. *Nature*, **266**, 318–323.

BRENOT, H., THEYS, N. *ET AL.* 2013. Support to Aviation Control Service (SACS): an online service for near real-time satellite monitoring of volcanic plumes. *Natural Hazards and Earth System Sciences Discussion*, **1**, 5935–6000, http://dx.doi.org/10.5194/ nhessd-1-5935-2013

BUCK, W. R. 2004. Consequences of asthenospheric variability on continental rifting. *In*: KARNER, G. D., TAYLOR, B., DRISCOLL, N. W. & KOHLSTEDT, D. L. (eds) *Rheology and Deformation of the Lithosphere at Continental Margins*. Columbia University Press, New York, 1–30.

BUCK, W. R., EINARSSON, P. & BRANDSDOTTIR, B. 2006. Tectonic stress and magma chamber size as controls on dike propagation: constraints from the 1975–1984 Krafla rifting episode. *Journal of Geophysical Research: Solid Earth*, **111**, B12404.

DAHM, T., HAINZL, S. & FISCHER, T. 2010. Bidirectional and unidirectional fracture growth during hydrofracturing: role of driving stress gradients. *Journal of Geophysical Research*, **115**, B12322.

DANIELS, K. A., BASTOW, I. D., KEIR, D., SPARKS, R. S. J. & MENAND, T. 2014. Thermal models of dyke intrusion during development of continent–ocean transition. *Earth and Planetary Science Letters*, **385**, 145–153, http://doi.org/10.1016/j.epsl.2013.09.018

DAVIES, A. G., CHIEN, S. *ET AL.* 2006. Monitoring active volcanism with the Autonomous Sciencecraft Experiment on EO-1. *Remote Sensing of Environment*, **101**, 427–446, http://dx.doi.org/10.1016/j.rse.2005.08.007

DAVIES, A. G., KESZTHELYI, L. P. & HARRIS, A. J. L. 2010. The thermal signature of volcanic eruptions on Io and Earth. *Journal of Volcanology and Geothermal Research*, **194**, 75–99, http://dx.doi.org/10.1016/j.jvolgeores.2010.04.009

DELANEY, J. R., KELLEY, D. S. *ET AL.* 1998. The quantum event of oceanic crustal accretion: impacts of diking at mid-ocean ridges. *Science*, **281**, 222–230.

DOUBRE, C., MANIGHETTI, I., DORBATH, C., DORBATH, L., JACQUES, E. & DELMOND, J. C. 2007a. Crustal structure and magmato-tectonic processes in an active rift (Asal-Ghoubbet, Afar, East Africa): 1. Insights from a 5-month seismological experiment. *Journal of Geophysical Research: Solid Earth*, **112**, B05405, http://dx.doi.org/10.1029/2005jb003940

DOUBRE, C., MANIGHETTI, I., DORBATH, L., DORBATH, C., BERTIL, D. & DELMOND, J. C. 2007b. Crustal structure and magmato-tectonic processes in an active rift (Asal-Ghoubbet, Afar, East Africa): 2. Insights from the 23-year recording of seismicity since the last rifting event. *Journal of Geophysical Research: Solid Earth*, **112**, B05406, http://dx.doi.org/10.1029/2006 jb004333

EBINGER, C., AYELE, A. *ET AL.* 2010. Length and time-scales of rift faulting and magma intrusion: the Afar Rifting Cycle from 2005 to present. *Annual Review of Earth and Planetary Sciences*, Annual Reviews, Palo Alto, **38**, 439–466.

EBINGER, C. J., VAN WIJK, J. & KEIR, D. 2013. The time scales of continental rifting: Implications for global processes. *In*: BICKFORD, M. E. (ed.) *The Web of Geological Sciences: Advances, Impacts, and Interactions*. Geological Society of America Special Papers, **500**, 371–396, http://doi.org/10.1130/2013.2500(11)

EINARSSON, P. & BRANDSDOTTIR, B. 1980. Seismological evidence for lateral magma intrusion during the July 1978 deflation of the Krafla volcano in NE Iceland. *Journal of Geophysics-Zeitschrift Fur Geophysik*, **47**, 160–165.

FARR, T. G. & KOBRICK, M. 2000. Shuttle radar topography mission produces a wealth of data. *Eos, Transactions American Geophysical Union*, **81**, 583–585, http://doi.org/10.1029/EO081i048p00583

FERGUSON, D. J., BARNIE, T. D. *ET AL.* 2010. Recent rift-related volcanism in Afar, Ethiopia. *Earth and Planetary Science Letters*, **292**, 409–418, http://dx.doi.org/10.1016/j.epsl.2010.02.010

FERGUSON, D. J., CALVERT, A. T., PYLE, D. M., BLUNDY, J. D., YIRGU, G. & WRIGHT, T. J. 2013. Constraining timescales of focused magmatic accretion and extension in the Afar crust using lava geochronology. *Nature Communications*, **4**, 1416, http://dx.doi.org/10.1038/ncomms2410

FIELD, L., BLUNDY, J., BROOKER, R. A., WRIGHT, T. & YIRGU, G. 2012a. Magma storage conditions beneath Dabbahu Volcano (Ethiopia) constrained by petrology,

seismicity and satellite geodesy. *Bulletin of Volcanology*, **74**, 981–1004, http://dx.doi.org/10.1007/s00445-012-0580-6

FIELD, L., BLUNDY, J., CALVERT, A. & YIRGU, G. 2012b. Magmatic history of Dabbahu, a composite volcano in the Afar Rift, Ethiopia. *Geological Society of America Bulletin*, **125**, 128–147, http://dx.doi.org/10.1130/b30560.1

GOLDSTEIN, R. M. & WERNER, C. L. 1998. Radar interferogram filtering for geophysical applications. *Geophysical Research Letters*, **25**, 4035–4038, http://dx.doi.org/10.1029/1998gl900033

GOLDSTEIN, R. M., ZEBKER, H. A. & WERNER, C. L. 1988. Satellite radar interferometry: two-dimensional phase unwrapping. *Radio Science*, **23**, 713–720, http://dx.doi.org/10.1029/RS023i004p00713

GRANDIN, R., SOCQUET, A. *ET AL.* 2009. September 2005 Manda Hararo-Dabbahu rifting event, Afar (Ethiopia): constraints provided by geodetic data. *Journal of Geophysical Research – Part B: Solid Earth*, **114**, B08404, http://dx.doi.org/10.1029/2008jb005843

GRANDIN, R., SOCQUET, A., JACQUES, E., MAZZONI, N., DE CHABALIER, J. B. & KING, G. C. P. 2010a. Sequence of rifting in Afar, Manda-Hararo rift, Ethiopia, 2005–2009: time–space evolution and interactions between dikes from interferometric synthetic aperture radar and static stress change modeling. *Journal of Geophysical Research: Solid Earth*, **115**, B10413, http://dx.doi.org/10.1029/2009jb000815

GRANDIN, R., SOCQUET, A., DOIN, M. P., JACQUES, E., DE CHABALIER, J. B. & KING, G. C. P. 2010b. Transient rift opening in response to multiple dike injections in the Manda Hararo rift (Afar, Ethiopia) imaged by time-dependent elastic inversion of interferometric synthetic aperture radar data. *Journal of Geophysical Research: Solid Earth*, **(1978–2012)**, 115(B9).

GRANDIN, R., JACQUES, E. *ET AL.* 2011. Seismicity during lateral dike propagation: insights from new data in the recent Manda Hararo-Dabbahu rifting episode (Afar, Ethiopia). *Geochemistry, Geophysics, Geosystems*, **12**, Q0AB08.

HAMLING, I. J., AYELE, A. *ET AL.* 2009. Geodetic observations of the ongoing Dabbahu rifting episode: new dyke intrusions in 2006 and 2007. *Geophysical Journal International*, **178**, 989–1003, http://dx.doi.org/10.1111/j.1365-246X.2009.04163.x

HAMLING, I. J., WRIGHT, T. J., CALAIS, E., BENNATI, L. & LEWI, E. 2010. Stress transfer between thirteen successive dyke intrusions in Ethiopia. *Nature Geoscience*, **3**, 713–717, http://dx.doi.org/10.1038/ngeo967

HAMLING, I. J., WRIGHT, T. J., CALAIS, E., LEWI, E. & FUKAHATA, Y. 2014. InSAR observations of post-rifting deformation around the Dabbahu rift segment, Afar, Ethiopia. *Geophysical Journal International*, **197**, 33–49.

HANKS, T. C. & KANAMORI, H. 1979. A moment magnitude scale. *Journal of Geophysical Research: Solid Earth*, **84**, 2348–2350, http://dx.doi.org/10.1029/JB084iB05p02348

HAYWARD, N. J. & EBINGER, C. J. 1996. Variations in the along-axis segmentation of the Afar Rift system. *Tectonics*, **15**, 244–257.

HEAD, J. W., WILSON, L. & SMITH, D. K. 1996. Mid-ocean ridge eruptive vent morphology and substructure: evidence for dike widths, eruption rates, and evolution of

eruptions and axial volcanic ridges. *Journal of Geophysical Research: Solid Earth*, **101**, 28265–28280, http://dx.doi.org/10.1029/96jb02275

HYVARINEN, A., KARHUNEN, J. & OJA, E. 2001. *Independent Component Analysis*. Wiley-Blackwell, New York.

JACQUES, E., RUEGG, J. C., LEPINE, J. C., TAPPONNIER, P., KING, G. C. P. & OMAR, A. 1999. Relocation of M ≥ 2 events of the 1989 Dobi seismic sequence in Afar: evidence for earthquake migration. *Geophysical Journal International*, **138**, 447–469, http://dx.doi.org/10.1046/j.1365-246X.1999.00881.x

KAO, H., JIAN, P. R., MA, K. F., HUANG, B. S. & LIU, C. C. 1998. Moment-tensor inversion for offshore earthquakes east of Taiwan and their implications to regional collision. *Geophysical Research Letters*, **25**, 3619–3622, http://dx.doi.org/10.1029/98gl02803

KEIR, D., STUART, G. W., JACKSON, A. & AYELE, A. 2006. Local earthquake magnitude scale and seismicity rate for the Ethiopian rift. *Bulletin of the Seismological Society of America*, **96**, 2221–2230, http://dx.doi.org/10.1785/0120060051

KEIR, D., HAMLING, I. J. *ET AL.* 2009. Evidence for focused magmatic accretion at segment centers from lateral dike injections captured beneath the Red Sea rift in Afar. *Geology*, **37**, 59–62.

KEIR, D., PAGLI, C., BASTOW, I. D. & AYELE, A. 2011. The magma-assisted removal of Arabia in Afar: evidence from dike injection in the Ethiopian rift captured using InSAR and seismicity. *Tectonics*, **30**, TC2008, http://dx.doi.org/10.1029/2010TC002785

KEIR, D., BASTOW, I. D., PAGLI, C. & CHAMBERS, E. L. 2013. The development of extension and magmatism in the Red Sea rift of Afar. *Tectonophysics*, **607**, 98–114, http://dx.doi.org/10.1016/j.tecto.2012.10.015

KLEIN, F. W. 2002. *User's guide to HYPOINVERSE-2000, a FORTRAN program to solve for earthquake locations and magnitudes*. US Geological Survey Open File Report, **02–171**.

MAKRIS, J. & GINZBURG, A. 1987. The Afar Depression – transition between continental rifting and sea-floor spreading. *Tectonophysics*, **141**, 199–214, http://dx.doi.org/10.1016/0040-1951(87)90186-7

MEDYNSKI, S., PIK, R. *ET AL.* 2013. Controls on magmatic cycles and development of rift topography of the Manda Hararo segment (Afar, Ethiopia): insights from cosmogenic ^{3}He investigation of landscape evolution. *Earth and Planetary Science Letters*, **367**, 133–145.

NASA 2014. *Aura OMI Sulphur Dioxide Data Product – OMSO2*, http://disc.sci.gsfc.nasa.gov/Aura/data-holdings/OMI/omso2_v003.shtml

OMI ROW ANOMALY TEAM 2012. *Background information about the Row Anomaly in OMI*, http://www.knmi.nl/omi/research/product/rowanomaly-background.php

RICHTER, C. F. 1935. An instrumental earthquake magnitude scale. *Bulletin of the Seismological Society of America*, **25**, 1–32.

RIVALTA, E. 2010. Evidence that coupling to magma chambers controls the volume history and velocity of laterally propagating intrusions. *Journal of Geophysical Research: Solid Earth*, **115**, B07203, http://dx.doi.org/10.1029/2009jb006922

RIVALTA, E., TAISNE, B., BUNGER, A. P. & KATZ, R. F. 2015. A review of mechanical models of dike

propagation: schools of thought, results and future directions. *Tectonophysics*, **638**, 1–42.

RIX, M., VALKS, P. *ET AL.* 2009. Satellite monitoring of volcanic sulfur dioxide emissions for early warning of volcanic hazards. *Selected Topics in Applied Earth Observations and Remote Sensing, IEEE Journal of*, **2**, 196–206, http://dx.doi.org/10.1109/jstars.2009.2031120

ROMAN, D. C. & CASHMAN, K. V. 2006. The origin of volcano-tectonic earthquake swarms. *Geology*, **34**, 457–460, http://doi.org/10.1130/G22269.1

ROSEN, P. A., HENSLEY, S., PELTZER, G. & SIMONS, M. 2004. Updated repeat orbit interferometry package released. *EOS, Transactions of the American Geophysical Union*, **85**, 47–47, http://dx.doi.org/10.1029/2004eo050004

RUEGG, J. C. & KASSER, M. 1987. Deformation across the Asal-Ghoubbet rift, Djibouti, uplift and crustal extension 1979–1986. *Geophysical Research Letters*, **14**, 745–748, http://dx.doi.org/10.1029/GL014i007p00745

RUEGG, J. C., LEPINE, J. C., TARANTOLA, A. & KASSER, M. 1979. Geodetic measurements of Rifting associated with a seismo-volcanic crisis in Afar. *Geophysical Research Letters*, **6**, 817–820.

SACS, 2010. *SO2 vertical column [DU] for the 21 May 2010 from Gome over North Africa*, http://sacs.aeronomie.be/nrt/Gome2Nrt/2010/05.orb/21/gome2_vcd20100521_207_lr.gif

SACS, 2012. *Support to Aviation Control Service Archive*, http://sacs.aeronomie.be/archive/month/index_VCD_month.php

STONE, J. V. 2004. *Independent Component Analysis*. MIT Press, MA.

TARASEWICZ, J., BRANDSDÓTTIR, B., WHITE, R. S., HENSCH, M. & THORBJARNARDÓTTIR, B. 2012. Using microearthquakes to track repeated magma intrusions beneath the Eyjafjallajökull stratovolcano, Iceland. *Journal of Geophysical Research: Solid Earth*, **117**, B00C06, http://dx.doi.org/10.1029/2011jb008751

TRYGGVASON, E. 1984. Widening of the Krafla fissure swarm during the 1975–1981 volcano-tectonic episode. *Bulletin Volcanologique*, **47**, 47–69, http://dx.doi.org/10.1007/bf01960540

UNGAR, S. G., PEARLMAN, J. S., MENDENHALL, J. A. & REUTER, D. 2003. Overview of the Earth Observing One (EO-1) mission. *IEEE Transactions on Geoscience and Remote Sensing*, **41**, 1149–1159, http://dx.doi.org/10.1109/tgrs.2003.815999

WRIGHT, T. J., EBINGER, C., BIGGS, J., AYELE, A., YIRGU, G., KEIR, D. & STORK, A. 2006. Magma-maintained rift segmentation at continental rupture in the 2005 Afar dyking episode. *Nature*, **442**, 291–294.

YANG, K., KROTKOV, N. A., KRUEGER, A. J., CARN, S. A., BHARTIA, P. K. & LEVELT, P. F. 2007. Retrieval of large volcanic SO_2 columns from the Aura Ozone monitoring instrument: comparison and limitations. *Journal of Geophysical Research: Atmospheres*, **112**, D24S43, http://dx.doi.org/10.1029/2007jd008825

ZHU, L. P. & RIVERA, L. A. 2002. A note on the dynamic and static displacements from a point source in multilayered media. *Geophysical Journal International*, **148**, 619–627, http://dx.doi.org/10.1046/j.1365-246X.2002.01610.x